

Gas gain and signal length measurements with a triple-GEM at different pressures of Ar-, Kr- and Xe-based gas mixtures^{*}

A. Orthen^{a,*}, H. Wagner^a, H.J. Besch^a, S. Martoiu^a,
R.H. Menk^b, A.H. Walenta^a, U. Werthenbach^a

^a*Universität Siegen, Fachbereich Physik, Emmy-Noether-Campus,
Walter-Flex-Straße 3, 57068 Siegen, Germany*

^b*ELETTRA, Sincrotrone Trieste, S.S. 14, km 163.5, Basovizza, 34012 Trieste,
Italy*

Abstract

We investigate the gas gain behaviour of a triple-GEM configuration in gas mixtures of argon, krypton and xenon with ten and thirty percent of carbon dioxide at pressures between 1 and 3 bar. Since the signal widths affect the dead time behaviour of the detector we present signal length measurements to evaluate the use of the triple-GEM in time-resolved X-ray imaging.

PACS: 51.10.+y; 51.50.+v; 29.40.Cs

Key words: Micro pattern gaseous detectors; GEM; Gas electron multiplier; Gas gain; Signal shape; Time-resolved X-ray imaging

1 Introduction

In the recent years the application range of GEMs (gas electron multipliers) [1] in detector development has been widened up. Besides the operation in detectors at high energy projects like HERA-B [2], COMPASS [3] or DIRAC

^{*} Work supported by the European Community (contract no. ERBFMGECT980104).

^{*} Corresponding author. Tel.: +49 271-740-3563; fax: +49 271-740-3533; e-mail: orthen@alwa02.physik.uni-siegen.de.



Fig. 1. Schematic cross section of the triple-GEM detector.

[4] the GEM is also used in gaseous photomultiplier development [5,6] or X-ray imaging detectors [7,8]. Thereby, the GEM is usually combined with other micro pattern devices like MSGCs [9,10], MGCs [11], micromegas [12] or MicroCAT [13]. Also the cascade of multiple GEMs has been tested extensively [14].

A triple-GEM cascade working as a detector for solar neutrino and dark matter search has been tested at high pressure of pure noble gases [15,16]. High pressure is also desired in photon detection to increase quantum efficiency. If pure noble gases are not explicitly needed it is helpful to add a quench gas fraction of up to some 10 % to the noble gases. This leads normally to smaller charge diffusion, shorter signal lengths and the possibility to obtain higher gas gains. Examinations of the gas gaining behaviour of alternative micro pattern devices like MSGCs [17] or the behaviour of a single GEM/MSGC-combination [18] in noble gas/quench gas environments show that the maximum gain drops with pressure.

The aim of our investigations is to test the performance of a triple-GEM detector at higher pressures of noble gas/quench gas mixtures to increase the quantum efficiency for photon detection in the energy range of 8–24 keV. We investigate the gas gain behaviour at different pressures and quench gas fractions. We examine the signal lengths which mainly affect the dead time. Besides space charge effects the dead time limits the rate capability.

2 Detector setup

The schematic setup of the triple-GEM detector is shown in Fig. 1. The individual GEM foils with dimensions of $6 \times 6 \text{ cm}^2$ are glued under slight tension to a 1 mm thick ceramic frame. The GEM type is characterised by a hole pitch of $140 \mu\text{m}$ and an optical transparency of 12 %; the hole shape is double-conical with an inner diameter of about $50 \mu\text{m}$ and an outer diameter of about $90 \mu\text{m}$. The holes are hexagonally arranged; the thickness of the GEM amounts to $60 \mu\text{m}$ including two copper layers of $5 \mu\text{m}$ each and a Kapton thickness of $50 \mu\text{m}$.

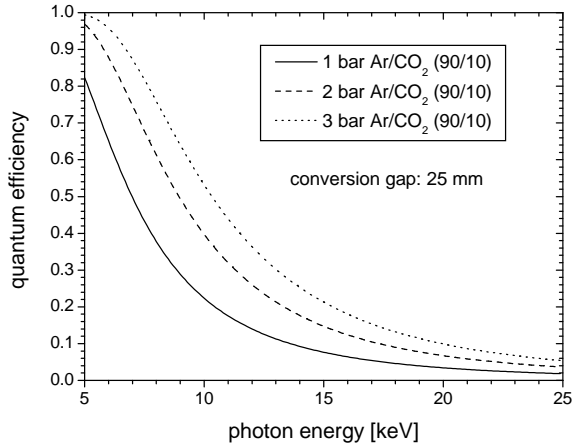


Fig. 2. Quantum efficiency as a function of photon energy at pressures between 1 and 3 bar of Ar/CO₂ (90/10) with a conversion gap of 25 mm.

We have set the distance between the GEMs to 2 mm. The lowermost GEM is mounted at a distance of 1 mm above the readout structure. Following the usual nomenclature we denote the applied electric field between the GEMs by *transfer field* and the field between the lowermost GEM and the readout structure by *induction field*. Above the GEM configuration a drift cage is mounted which provides a homogeneous *drift field* in the conversion gap of 27 mm.

For the gas gain measurements (s. section 3) a copper anode with a size corresponding to the GEMs has been used. The signal examination (s. section 4) has been carried out with a smaller copper anode ($\approx 1 \text{ cm}^2$) to reduce the capacitance and therefore the noise of the preamplifier.

The 1 mm thick carbon fibre entrance window of the pressure vessel accepts pressures up to about 3 bar. Figs. 2–4 show the quantum efficiency of a detector filled with Ar/CO₂, Kr/CO₂ and Xe/CO₂ (90/10) with a typical conversion gap of 25 mm. To achieve high quantum efficiency for photon detection in the energy range of 5–14 keV xenon gas mixtures are preferably used. For photons in the energy range of about 14–24 keV quantum efficiency increases by the use of krypton with a K-shell energy of 14.3 keV. Higher quench gas fractions, showed as an example for Xe/CO₂ (70/30) in Fig. 4, decrease quantum efficiency.

3 Gas gain measurements

In the following section we present results of gas gain measurements in the triple-GEM configuration. The effective gain G_{eff} is experimentally determined by the quotient of the measured current at the anode I_{anode} and the “incoming”

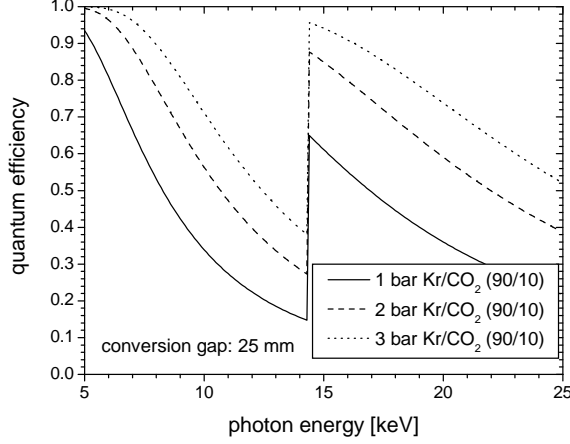


Fig. 3. Quantum efficiency as a function of photon energy at pressures between 1 and 3 bar of Kr/CO₂ (90/10) with a conversion gap of 25 mm.

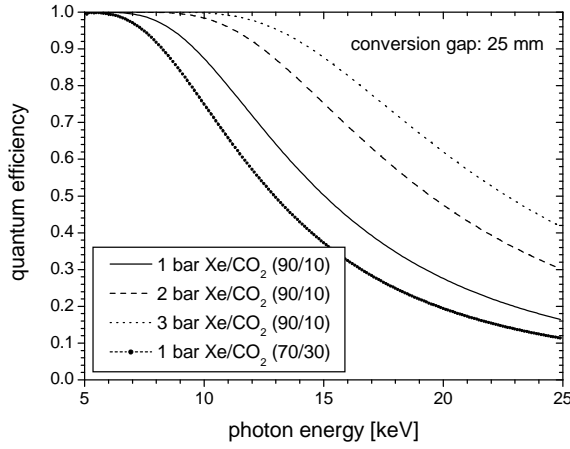


Fig. 4. Quantum efficiency as a function of photon energy at pressures between 1 and 3 bar of Xe/CO₂ (90/10) and 1 bar of Xe/CO₂ (70/30) with a conversion gap of 25 mm.

current I_0 :

$$G_{\text{eff}} = \frac{I_{\text{anode}}}{I_0} . \quad (1)$$

The current

$$I_0 = R e \frac{E_\gamma}{W} \quad (2)$$

is determined by the conversion rate R of the X-ray photons in counting mode of the detector, by the photon energy E_γ and by the average energy required to produce one electron-ion pair in the gas W ; e denotes the elementary charge.

In fact, the incoming current I_0 is overestimated – at least at small drift fields and high gas pressures – because of charge losses due to recombination and attachment in the conversion region. This charge loss effect, which is mainly a

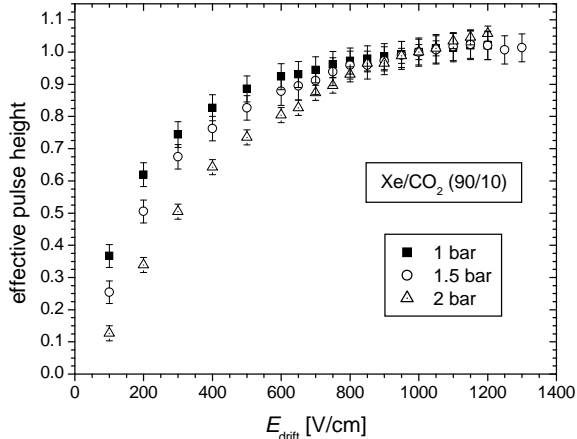


Fig. 5. Effective pulse height as a function of the applied drift field in Xe/CO₂ (90/10) for a transfer field of 2500 V/cm and an induction field of 3000 V/cm.

three-body process and therefore increases with the square of the gas pressure, is shown as an example in Fig. 5 in a Xe/CO₂ (90/10) gas mixture at pressures between 1 and 2 bar. At drift fields larger than about 1000 V/cm the effective pulse height reaches a plateau. In this region attachment and recombination is negligible and the incoming current I_0 is described correctly by Eq. (2).

Since the maximum voltage applied to the drift cathode was restricted by the detector geometry to around $-(6000 \pm 500)$ V we have chosen a drift field of 400 V/cm to prevent the detector from sparking at the drift cathode and to have enough margin to increase more crucial potentials like GEM operation voltages. The transfer fields have been chosen to 2500 V/cm, and we have applied an induction field of 3000 V/cm to avoid full discharge propagation [19]. Furthermore, we have set the GEM voltages such, that the uppermost GEM voltage is 10 % higher than the voltage of the middle GEM; the lowermost GEM is set to an operation voltage 10 % smaller than the “reference” voltage of the middle GEM ΔU_{GEM2} . This setting assures minimum discharge rates [19]. The sum of all applied GEM voltages always amounts to $3 \Delta U_{\text{GEM2}}$.

For illumination with X-ray photons we have used a ⁵⁵Fe source, emitting photons with an energy of 5.9 keV and with a rate of 41 kHz collimated to about 28 mm². During all measurements the gas gain was found to decrease as a function of illumination time and photon rate most likely due to charging of the insulating Kapton in the GEM. The charging is dependent on illumination time and position, photon flux and dryness of the Kapton surface. We can not explain why in our setup the gain decreased as a function of time, whereas gain increased in measurements of other groups (i.e. [14],[20]). The problem of charging of the Kapton and hence of the time and rate dependent gas gaining behaviour may be solved by using carbon coated gas electron multipliers [21]. In our case, however, all data has been taken after an equilibrium state had been reached.

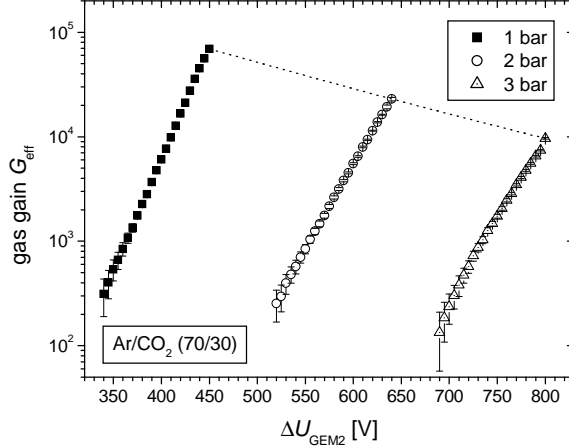


Fig. 6. Effective gas gain as a function of the applied voltage at the middle GEM ΔU_{GEM2} in Ar/CO₂ (70/30) at pressures of 1, 2 and 3 bar. The voltages applied to the first and third GEM have been changed proportionally.

The gas gain measurements were limited by sparks. We stopped the measurements at spark rates $\gtrsim 2$ sparks/min, which is rather an arbitrary limit. Important, however, is the stable detector operation at slightly lower voltages and hence lower gas gains.

3.1 Gas gain in Ar/CO₂ (70/30)

Although quantum efficiency in argon mixtures for photon detection in the higher energy range is small compared to krypton or xenon mixtures we have carried out gas gain measurements in Ar/CO₂ (70/30) to compare the results to those achieved with Kr- and Xe-mixtures. The measured effective gain, shown in Fig. 6, exceeds $6 \cdot 10^4$ at standard pressure. The maximum gas gain achievable decreases with pressure, but we have still obtained a maximum gain of about 10^4 at a pressure of 3 bar.

3.2 Gas gain in Kr/CO₂ mixtures

We have investigated two Kr-mixtures with different CO₂ fractions of 30 % (see Fig. 7) and 10 % (see Fig. 8), respectively. In both mixtures the effective gain exceeds 10^4 up to pressures of 2 bar. Nevertheless, a quench gas fraction of 30 % is not well suited for operation at pressures > 2 bar where we obtained a strong decrease in gas gain to about 200. In contrast to that still large gas gains in the order of $5 \cdot 10^3$ are possible with a carbon dioxide fraction of 10 %.

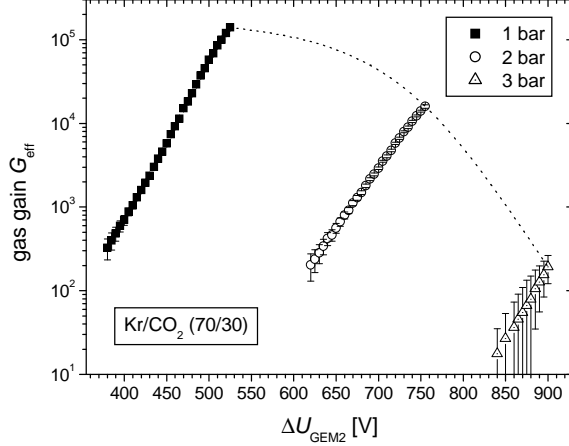


Fig. 7. Effective gas gain as a function of the applied voltage at the middle GEM ΔU_{GEM2} in Kr/CO₂ (70/30) at pressures of 1, 2 and 3 bar.

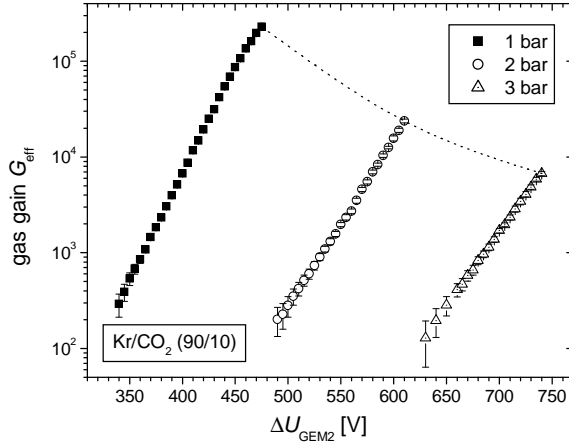


Fig. 8. Effective gas gain as a function of the applied voltage at the middle GEM ΔU_{GEM2} in Kr/CO₂ (90/10) at pressures of 1, 2 and 3 bar.

3.3 Gas gain in Xe/CO₂ mixtures

The use of Xe-based gas mixtures offers the largest quantum efficiency for photon detection in the energy range between 5 and 14 keV. Results of gas gain measurements for Xe/CO₂ (70/30) and Xe/CO₂ (90/10) are shown in Fig. 9 and Fig. 10. Like for Kr-gas mixtures an amount of 10 % carbon dioxide enables operation with gas gains $> 10^3$ at pressures above 2 bar. High quencher fractions are not well suited for pressure operation with xenon.

3.4 Homogeneity

Figure 11 shows the relative effective gain measured along the vertically centred x -axis. Gain variations of up to 25 % become obvious. These local vari-

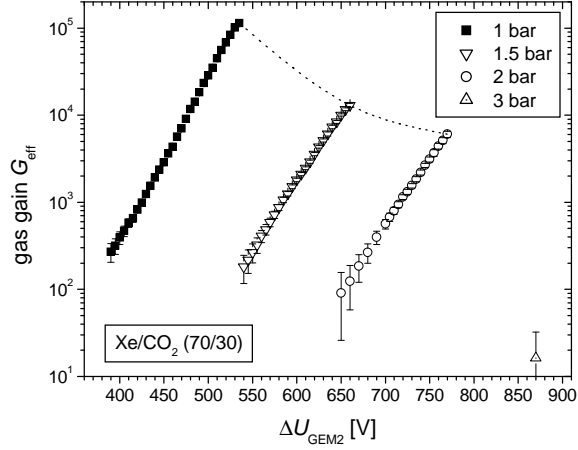


Fig. 9. Effective gas gain as a function of the applied voltage at the middle GEM ΔU_{GEM2} in Xe/CO₂ (70/30) at pressures of 1, 1.5, 2 and 3 bar.

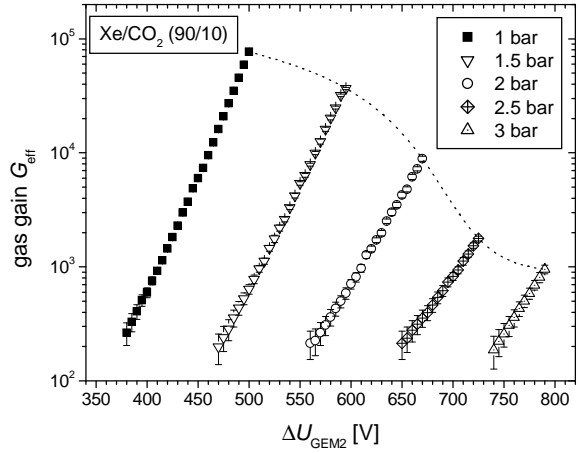


Fig. 10. Effective gas gain as a function of the applied voltage at the middle GEM ΔU_{GEM2} in Xe/CO₂ (90/10) at pressures of 1, 1.5, 2, 2.5 and 3 bar.

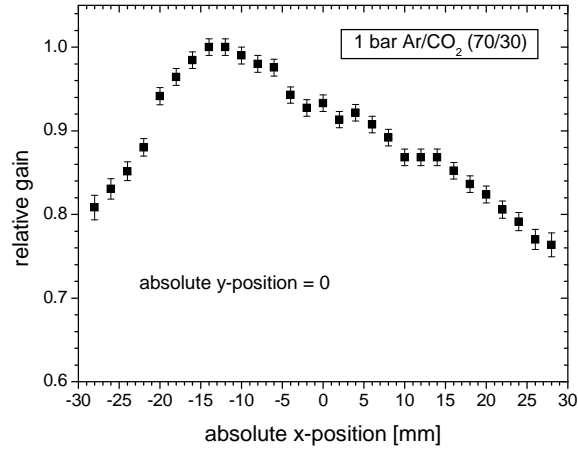


Fig. 11. Relative effective gain along the vertically centred x -axis of the detector in Ar/CO₂ (70/30) at standard pressure.

ations are mainly due to two aspects: First, the GEMs, themselves, produce intrinsic gain inhomogeneities because of geometry variations. Furthermore, the distances between the individual GEMs and the distance between undermost GEM and anode are not constant over all the detector area, which leads to transfer and induction field inhomogeneities and finally to variations in the charge transfer behaviour and in the effective gas gain of the GEMs [13].

3.5 Discussion

We have measured the gas gain behaviour at different pressures of argon, krypton and xenon with additions of 10 % and 30 % of carbon dioxide. A strong influence of the quench gas fraction on the gas gain behaviour becomes obvious. It is definitely a non-trivial task to optimise the fraction of quencher at a given pressure with respect to a maximum achievable gain due to a complicated interplay of these parameters.

Generally, the maximum gas gain of the triple-GEM achievable in slightly quenched noble gas mixtures is higher than in pure noble gases (compare to Refs. [15,16]). At standard pressure the krypton and xenon gas mixtures with 10 % CO₂ behave relatively similarly to the mixtures with 30 % CO₂. Increasing gas pressure leads to a larger deviation in maximum achievable gas gain. Higher pressure demands obviously for smaller quench gas fractions.

The strong influence of the quencher fraction indicates, that a stable avalanche process is not only based on electron-induced ionization of gas atoms. The UV-photons which are produced in the avalanche development may contribute noticeably to the multiplication procedure. With increasing pressure and constant (or even larger) quench gas fraction the mean free path of the UV-photons is decreasing. For instance, the deterioration in energy resolution in a MWPC is stopped when a very small quench gas fraction of only 2 % at very high pressures (up to 30 bar) is added to argon [22]. However, still smaller fractions of quenching gas lead to an unsafe operation of the detector. We suppose, that the triple-GEM detector shows a comparable behaviour. It should be considered to use very small quench gas fractions of a few percent for really high pressure operation.

A good choice for photon detection with the triple-GEM is the use of Kr/CO₂ or Xe/CO₂ (90/10), depending on the energy range, at pressures between 1 and 2 bar. Gas gains of $5 \cdot 10^3$ can be easily reached without sparking.

4 Signal length investigations

We have studied the dependence of the anode signal shape on GEM voltage, induction field, transfer field and drift field for all gas mixtures and several pressures since the dead time behaviour of the detector is mainly determined by the signals lengths. The copper readout anode for these measurements has a size of $1 \times 1 \text{ cm}^2$. The integrating preamplifier and the shaper including a pole-zero filter to cancel the pole of the integrating first stage are in-house developments. The gaussian-like δ -response of this amplification system has a width of 15 ns (fwhm) due to bandwidth limitations.

Basically, the anode signal shape is determined by two aspects:

- (1) A spatially δ -like distributed electron cluster moving from the bottom side of the undermost GEM towards the readout structure induces a box-shaped current at both involved electrodes if the electric field and therefore the electron drift velocity in the region of interest is assumed to be constant [23]. The copper-clad bottom side of the GEM shields all currents induced by charge movements appearing above this electrode; especially the slow ions do not contribute to the signal shape, which is, however, the case for micromegas or MicroCAT detectors [24,25]. The crucial parameters for the width t_w of the box-shaped current are the electron drift velocity v_e in the electric field of the induction region and the distance d between the bottom side of the GEM and the anode which amounts to 1 mm in our case:

$$t_w = \frac{d}{v_e}. \quad (3)$$

- (2) The longitudinal diffusion σ_l of the primary produced electrons (photo-electron plus subsequently produced about 300 electrons for 8 keV photons in argon) in the conversion region leads to a temporal gaussian smearing of the above mentioned box function, mathematically expressed by a convolution of box and gauss function. The width of the gaussian

$$\sigma_t = \left(\sigma_{l0} \sqrt{l} \right) / v_e \quad (4)$$

is determined by the longitudinal diffusion coefficient σ_{l0} and the electron drift velocity v_e in the applied drift field and gas mixture used and finally by the mean drift path $\left(\sqrt{l} \right)^2$ of the primary produced electrons, which is dependent on photon energy, conversion gap and photoelectric absorption coefficient of the gas. Additionally, the longitudinal electron diffusion in the two transfer regions between the GEMs and in the induction region between undermost GEM and anode contribute to the temporal smearing

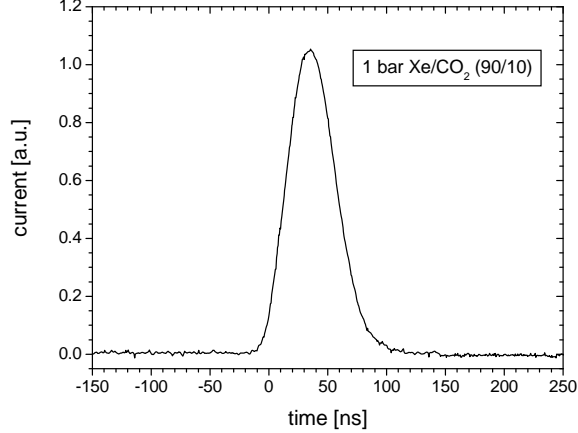


Fig. 12. Measured anode signal shape at a large drift field of 1000 V/cm in 1 bar Xe/CO₂ (90/10).

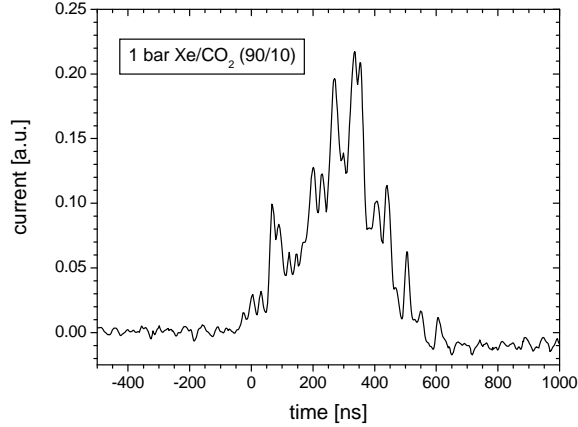


Fig. 13. Measured anode signal shape at a small drift field of 200 V/cm in 1 bar Xe/CO₂ (90/10).

σ_t . In our simulation this contribution has also been taken into account.

For most gas mixtures and pressures in our detector setup the temporal diffusion spreading (compare to Eq. (4)) is the main contribution which leads to a very much gaussian-like signal shape. Fig. 12 shows a typical signal obtained at a high drift field of 1000 V/cm at standard pressure. At smaller drift fields the signal shape looks differently (s. Fig. 13). The signal shape is not continuous anymore; single electron clusters reach the anode one by one, but still the gaussian character is well visible. We have measured the full width half maximum (fwhm) of the anode signals and the δ -response of the preamplifier with a digital oscilloscope, afterwards averaging the widths of several signals.

Due to the gaussian signal shape and the gaussian δ -response of the preamplifier/shaper-system the real signal length can be calculated to be the width of

the deconvolution of both gaussians:

$$\Delta_{\text{sig-real}}^2 = \Delta_{\text{sig-meas}}^2 - \Delta_{\delta\text{-response}}^2, \quad (5)$$

where Δ is the full width half maximum of the signal. In case the measured signal shape is not gaussian (which means that the main contribution of the signal is due to the electron induced box-shaped current, which is true for very small induction fields (s. section 4.2)) Eq. (5) is no longer valid. But in this case the measured signal width is very much larger than the width of the δ -response ($\Delta_{\text{sig-meas}} \gg \Delta_{\delta\text{-response}}$) and therefore the real signal width can be determined to be $\Delta_{\text{sig-real}} \approx \Delta_{\text{sig-meas}}$.

Despite most gas properties are E/p -dependent all measurements have been performed with a constant transfer field of 2500 V/cm and a constant induction field of 3000 V/cm even at high pressure if not noted otherwise, since these electric fields ensure maximum electron transparency of the GEM. The ^{55}Fe source has been collimated to about 12 mm²; photons were emitted with a rate of a few hundred Hz. We have carried out all signal width simulations only for 1 bar Ar/CO₂ (70/30), where experimental data on drift velocities [26] and simulated data on longitudinal diffusion [27,28] have been used.

4.1 Influence of GEM operation voltage

We have detected no influence of the GEM voltage on the signal length. The range of the investigated GEM voltages was limited by the dynamic range of the preamplifier. Anyway, the setting of the GEM voltage is determined by the desired gas gain and is therefore no freely adjustable parameter for optimisation of the signal lengths.

4.2 Influence of the induction field

The contribution of the width of the box-shaped current to the total width of the signal increases for very small induction fields due to a decreasing electron drift velocity (compare to Eq. (3)). Three-dimensional field calculations with Maxwell [29] using a geometry of 1 mm transfer gap, the 60 μm thick GEM foil and 1 mm induction gap (the geometry of the GEM and more simulation details are described in Ref. [13]) show that the electric field in the induction region along the symmetry axis of a GEM hole is larger than the quotient $E = U_{\text{GEM-bottom}}/d$ of the applied voltage on the bottom side of the GEM $U_{\text{GEM-bottom}}$ and the distance d between GEM bottom and anode. This effect is some relict due to the very high electric field in the holes. To determine the

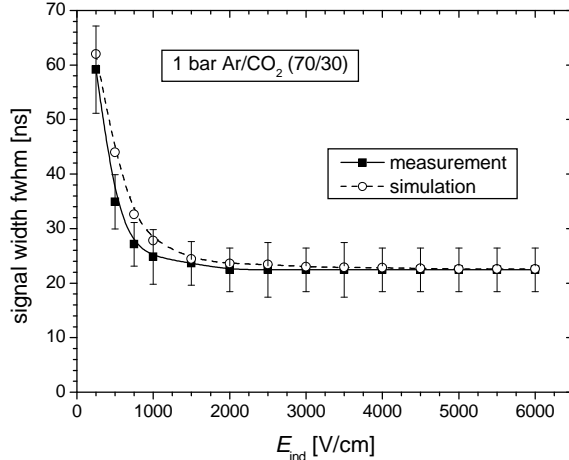


Fig. 14. Comparison between measured and simulated signal widths (fwhm) as a function of the induction field in 1 bar Ar/CO₂ (70/30) with a constant drift field of $E_{\text{drift}} = 900$ V/cm.

width of the electron induced box-shaped current we have used a parametrisation of the electron drift velocity, calculated by the Magboltz program [27,28], up to electric fields of 20 kV/cm. An average drift velocity in the induction region has been calculated and the box function is convoluted with a gaussian, describing the diffusion spreading. The results of this simulation and the comparison to experiment is shown in Fig. 14. A good agreement especially for induction fields ≥ 1 kV/cm becomes obvious. At induction fields larger than about 2000 V/cm the influence of the box-shaped current becomes negligible compared to the contribution of the temporal electron diffusion in the conversion region.

4.3 Influence of the transfer field

For this study both transfer fields between GEM1 and GEM2 and between GEM2 and GEM3 have been changed at the same time. The measured results are shown in Fig. 15. Transfer fields smaller than 2500 V/cm result in a slight increase of the signal width which can be explained by smaller electron drift velocities in the transfer regions and hence a larger diffusion spreading (compare to Eq. (4)). At larger transfer fields the signal width reaches a plateau. Higher pressure reflects smaller electron drift velocities and therefore larger signal widths.

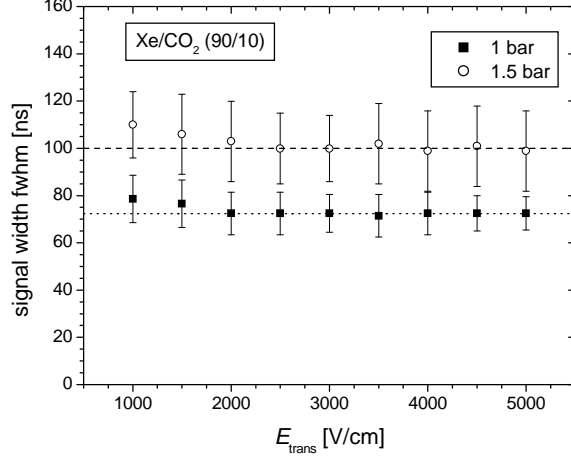


Fig. 15. Signal widths (fwhm) as a function of the transfer field between the uppermost and the middle and between the middle and the undermost GEM in 1 and 1.5 bar Xe/CO₂ (90/10) with a constant drift field of $E_{\text{drift}} = 1000$ V/cm.

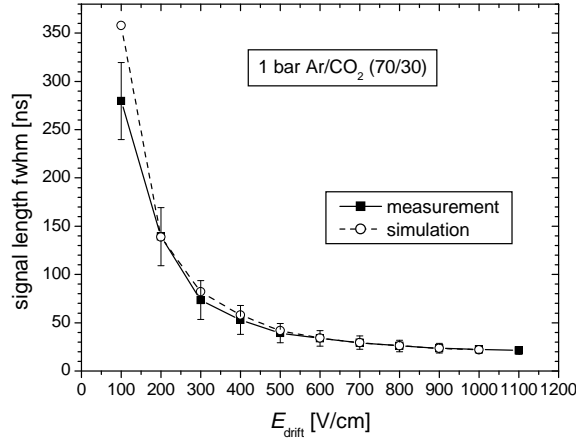


Fig. 16. Comparison between measured and simulated signal widths (fwhm) as a function of the drift field in 1 bar Ar/CO₂ (70/30).

4.4 Influence of the drift field

This section contains an intensive investigation of the influence of the applied drift field on the signal width. The comparison between measurement and simulation (see Fig. 16) shows a good agreement for drift fields $\gtrsim 200$ V/cm. The signal width measurements at small drift fields are very difficult due to the clustered signal shape (see Fig. 13). Therefore, the error is relatively large when determining these signal lengths. Furthermore, a large part of the primary produced electrons is lost due to recombination and attachment at low drift fields (compare to Fig. 5) and thus decreasing the signal-to-noise ratio.

The measured signal widths for different gas mixtures and gas pressures are

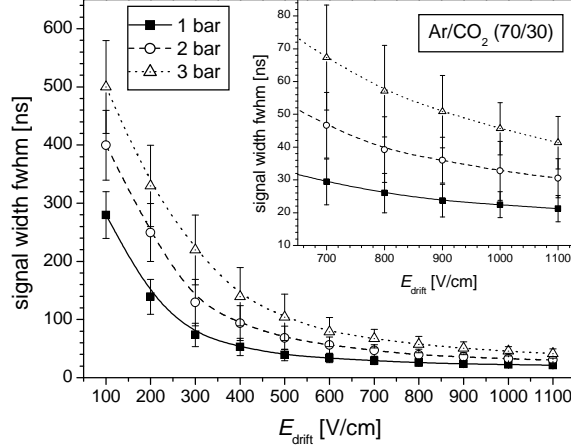


Fig. 17. Measured signal widths (fwhm) as a function of the drift field in 1, 2 and 3 bar Ar/CO₂ (70/30).

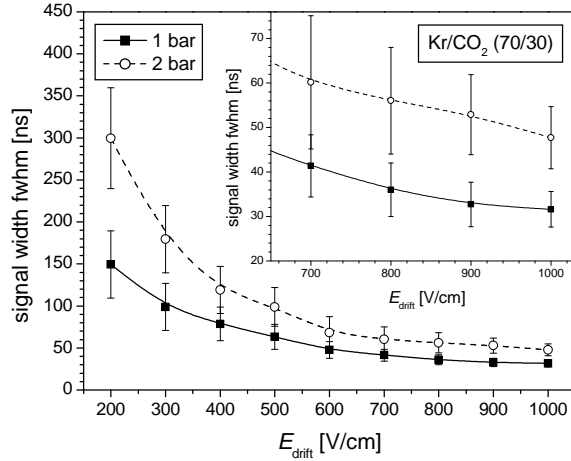


Fig. 18. Measured signal widths (fwhm) as a function of the drift field in 1 and 2 bar Kr/CO₂ (70/30).

shown in Figs. 17–21. Generally, high drift fields are needed to produce short signals. We were limited to about 1000–1200 V/cm due to sparking at the drift cathode. The fastest signals with a signal length of < 25 ns (fwhm) are produced in the argon mixture at standard pressure (see Fig. 17). Larger pressure always increases the signal width due to decreasing drift velocities in induction and conversion region and thus an increasing temporal smearing. But even in 1.5 bar Xe/CO₂ (90/10) the signal width does not exceed 60 ns (fwhm) at a drift field of 1100 V/cm.

4.5 Discussion

In our detector setup the drift field has the most crucial influence on the signal length although for smaller conversion regions this parameter becomes

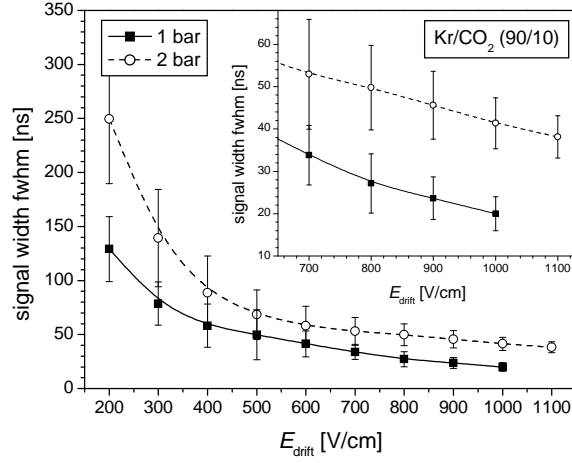


Fig. 19. Measured signal widths (fwhm) as a function of the drift field in 1 and 2 bar Kr/CO₂ (90/10).

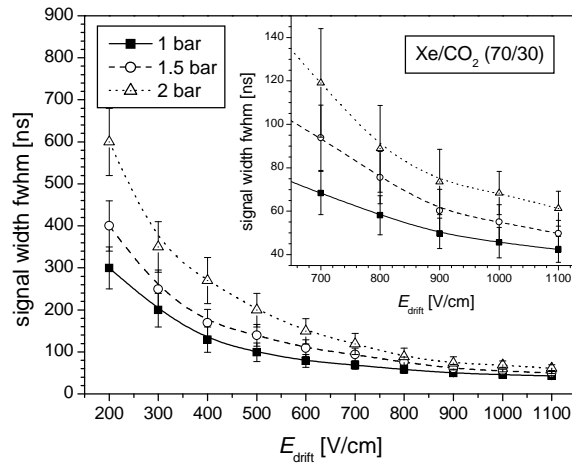


Fig. 20. Measured signal widths (fwhm) as a function of the drift field in 1, 1.5 and 2 bar Xe/CO₂ (70/30).

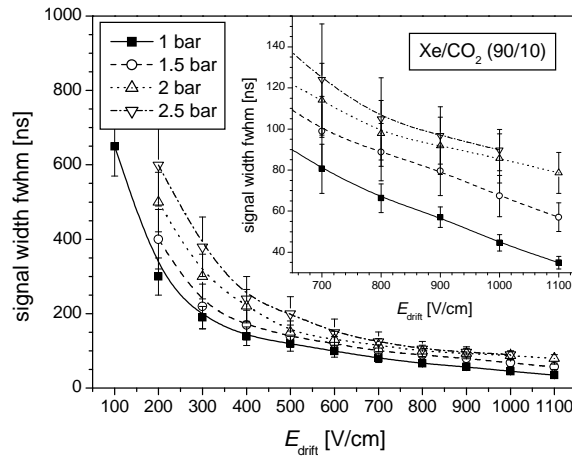


Fig. 21. Measured signal widths (fwhm) as a function of the drift field in 1, 1.5, 2 and 2.5 bar Xe/CO₂ (90/10).

less important due to smaller longitudinal electron diffusion. The drift field should be chosen as large as allowed by the detector setup. However, the drift field should not be too high ($\lesssim 2$ kV/cm) because the uppermost GEM loses transparency for too large drift fields [14]. Transfer and induction fields $\gtrsim 2$ kV/cm minimise the widths of the signal. If, however, the contribution of the electron induced box-shaped current becomes noticeable the distance between the undermost GEM and the anode can be reduced, i.e. to 0.5 mm. This should suppress this effect. The GEM operation voltage, which is mainly determined by the desired gas gain, does not influence the signal widths visibly.

5 Conclusion

We have measured the gas gain in a triple-GEM geometry for pressures up to 3 bar of Ar/CO₂ (70/30), Kr/CO₂ (70/30), Kr/CO₂ (90/10), Xe/CO₂ (70/30) and Xe/CO₂ (90/10). At a pressure > 2 bar the addition of 10 % of carbon dioxide to the noble gases leads to higher maximum gas gains compared to noble gases mixed with 30 % quench gas. Too large amounts of quench gas seem to disturb operation at high pressure and is therefore not preferable. Generally, we have obtained that the quench gas fraction should decrease with pressure.

Compared to the geometry of MicroCAT- or micromegas-detectors the triple-GEM-detector offers faster signals since only the electrons and not the slow ions contribute to the signal shape at the anode. The measured signal lengths at high drift fields in all gas mixtures and pressures investigated are smaller than about 100 ns (fwhm). If transfer and induction fields exceed 2 kV/cm the signal widths get to minimum.

Provided that the signal width is mainly determined by the temporal diffusion of the primary electrons in the conversion region further optimisation with respect to an increased high rate behaviour can be performed with exact knowledge of photon energy and desired quantum efficiency by reducing the conversion gap (compare to Figs. 2–4). For example, with a desired quantum efficiency of 90 % for 8 keV-photons in 1.5 bar Xe/CO₂ (90/10) it is sufficient to provide a conversion gap of 11 mm with mean drift path $(\sqrt{l_{11}})^2$ instead of 27 mm with mean drift path $(\sqrt{l_{27}})^2$ used for measurements described in this paper. Hence, the longitudinal diffusion and consequently the signal width will decrease by a factor of $\sqrt{l_{27}} / \sqrt{l_{11}} \approx 1.8$.

In combination with the resistive readout structure [30] it is proposed to integrate about 90 % of the charge to achieve optimum spatial resolution [31]. Compared to the signal length fwhm, presented here, the charge integra-

tion time from 5% to 95% of the original signal can be calculated to be $\tau_{5-95\%} \approx 1.4 \tau_{\text{fwhm}}$. Due to charge diffusion on the readout structure the charge integration time for signals with a width of $\tau_{5-95\%} = 92$ ns is stretched to about $\tau_{\text{rs:5-95\%}} = 150$ ns.

Acknowledgements

We are grateful to the inner tracker group of the HERA-B collaboration for providing several GEM foils. We thank C. Fiorini for providing the preamplifier design.

References

- [1] F. Sauli, Nucl. Instr. and Meth. A 386 (1997) 531.
- [2] T. Zeuner, Nucl. Instr. and Meth. A 446 (2000) 324.
- [3] B. Ketzer, M.C. Altunbas, K. Dehmelt, J. Ehlers, J. Friedrich, B. Grube, S. Kappler, I. Konorov, S. Paul, A. Placci, L. Ropelewski, F. Sauli, L. Schmitt, F. Simon, IEEE Transactions on Nuclear Science, Volume 49 (2002), 2403.
- [4] B. Adeva et al., *DIRAC: A High Resolution Spectrometer for Pionium Detection*, submitted to Nucl. Instr. and Meth.
- [5] A. Buzulutskov, A. Breskin, R. Chechik, G. Garty, F. Sauli, L. Shekhtman, Nucl. Instr. and Meth. A 443 (2000) 164.
- [6] A. Buzulutskov, A. Breskin, R. Chechik, G. Garty, F. Sauli, L. Shekhtman, Nucl. Instr. and Meth. A 442 (2000) 68.
- [7] M. Li, M.S. Dixit, P. Johns, Nucl. Instr. and Meth. A 471 (2001) 215.
- [8] S. Bachmann, S. Kappler, B. Ketzer, T. Müller, L. Ropelewski, F. Sauli, E. Schulte, Nucl. Instr. and Meth. A 478 (2002) 104.
- [9] Y. Benhammou, J.M. Brom, J.C. Fontaine, D. Huss, F. Jeanneau, A. Lounis, I. Ripp-Baudot, A. Zghiche, Nucl. Instr. and Meth. A 419 (1998) 400.
- [10] O. Baruth, S. Keller, U. Werthenbach, G. Zech, T. Zeuner, Nucl. Instr. and Meth. A 454 (2000) 272.
- [11] P. Fonte, V. Peskov, B.D. Ramsey, Nucl. Instr. and Meth. A 419 (1998) 405.
- [12] S. Kane, J. May, J. Miyamoto, I. Shipsey, *A study of micromegas with preamplification with a single GEM*, Proceeding for the International conference on advanced technology and particle physics, Villa Olmo, Como, Italy, Oct 15-19 (2001), submitted to Nucl. Phys. B.

- [13] A. Orthen, H. Wagner, H.J. Besch, R.H. Menk, A.H. Walenta, U. Werthenbach, Nucl. Instr. and Meth. A 500 (2003) 163.
- [14] S. Bachmann, A. Bressan, L. Ropelewski, F. Sauli, A. Sharma, D. Mörmann, Nucl. Instr. and Meth. A 438 (1999) 376.
- [15] A. Bondar, A. Buzulutskov, L. Shekhtman, Nucl. Instr. and Meth. A 481 (2002) 200.
- [16] A. Bondar, A. Buzulutskov, L. Shekhtman, V. Snopkov, A. Vasiljev, Nucl. Instr. and Meth. A 493 (2002) 8.
- [17] L. Shekhtman, F. Angelini, R. Bellazzini, A. Brez, M.M. Massai, G. Spandre, M.R. Torquati, Proceedings of the European Workshop on X-Ray Detectors for Synchrotron Radiation Sources. Aussois (1991) 96.
- [18] A. Bondar, A. Buzulutskov, F. Sauli, L. Shekhtman, Nucl. Instr. and Meth. A 419 (1998) 418.
- [19] S. Bachmann, A. Bressan, M. Capeáns, M. Deutel, S. Kappler, B. Ketzler, A. Polouektov, L. Ropelewski, F. Sauli, E. Schulte, L. Shekhtman, A. Sokolov, Nucl. Instr. and Meth. A 479 (2002) 294.
- [20] R. Bouclier, W. Dominik, M. Hoch, J.-C. Labbé, G. Million, L. Ropelewski, F. Sauli, A. Sharma, G. Manzin, Nucl. Instr. and Meth. A 396 (1997) 50.
- [21] S. Beirle, U. Werthenbach, G. Zech, T. Zeuner, Nucl. Instr. and Meth. A 423 (1999) 297.
- [22] T.G. Feige, Diploma Thesis, Siegen (1995).
- [23] V. Radeka, Ann. Rev. Nucl. Part. Sci. 38 (1988) 217.
- [24] J.P. Cussonneau, M. Labalme, P. Lautridou, L. Luquin, V. Metivier, A. Rahmani, V. Ramillien, T. Reposeur, Nucl. Instr. and Meth. A 419 (1998) 452.
- [25] A. Sarvestani, H.J. Besch, M. Junk, W. Meissner, N. Sauer, R. Stiehler, A.H. Walenta, R.H. Menk, Nucl. Instr. and Meth. A 410 (1998) 238.
- [26] C.M. Ma et al., MIT Technical Report 129 (1982), in: J. Fehlmann, G. Viertel, *Compilation of Data for Drift Chamber Operation*, ETH-Report (1983).
- [27] S.F. Biagi, Nucl. Instr. and Meth. A 421 (1999) 234.
- [28] Magboltz, CERN Transport of Electrons in Gas Mixtures Computation Program written by S.F. Biagi, Version 2 (2002).
- [29] Maxwell 3D Field Simulator Version 5.0.04, Ansoft Corporation, Pittsburgh, PA USA (2002).
- [30] H.J. Besch, M. Junk, W. Meissner, A. Sarvestani, R. Stiehler, A.H. Walenta, Nucl. Instr. and Meth. A 392 (1997) 244.
- [31] H. Wagner, H.J. Besch, R.H. Menk, A. Orthen, A. Sarvestani, A.H. Walenta, H. Walliser, Nucl. Instr. and Meth. A 482 (2002) 334.